Non-reciprocal behavior of one-dimensional piezoelectric structures with space-time modulated electrical boundary conditions

Charles Croënne, Jerome O. Vasseur, Olivier Bou Matar, Anne-Christine Hladky, Bertrand Dubus

Journal of Applied Physics

Non-reciprocal behavior of one-dimensional piezoelectric structures with space-time modulated electrical boundary conditions

Cite as: J. Appl. Phys. **126**, 145108 (2019); https://doi.org/10.1063/1.5110869
Submitted: 21 May 2019 . Accepted: 26 September 2019 . Published Online: 10 October 2019

C. Croënne, J. O. Vasseur, O. Bou Matar, A.-C. Hladky-Hennion, and B. Dubus

AIP Publishing

Journal of Applied Physics ARTICLE scitation.org/journal/jap

Non-reciprocal behavior of one-dimensional piezoelectric structures with space-time modulated electrical boundary conditions

Cite as: J. Appl. Phys. **126**, 145108 (2019); doi: 10.1063/1.5110869
Submitted: 21 May 2019 · Accepted: 26 September 2019 ·
Published Online: 10 October 2019

C. Croënne,[a] J. O. Vasseur, O. Bou Matar, A.-C. Hladky-Hennion, and B. Dubus

AFFILIATIONS

Univ. Lille, CNRS, Centrale Lille, ISEN, Univ. Valenciennes, UMR 8520—IEMN, F-59000 Lille, France

[a]charles.croenne@isen.fr

ABSTRACT

Propagation of longitudinal acoustic waves in a one-dimensional piezoelectric structure with space-time modulated electrical boundary conditions is investigated. An analytical model allowing the calculation of eigenmodes for spatially continuous shifts of electrical boundary conditions is compared with finite difference time domain simulation results for a discrete set of time-varying spatially fixed conditions. Both models predict that such a structure behaves as a nonreciprocal device exhibiting unidirectional propagation properties in some frequency ranges. The modulus and direction of the modulation speed vector strongly affect this nonreciprocal behavior. Moreover, other nonlinear phenomena such as frequency up and down conversions, wave packet distortion, and parasitic echoes occurring in such systems are investigated in detail. The importance of these phenomena is discussed in the context of nonlinear acoustic wave-based components for radio-communication systems.

I. INTRODUCTION

In his pioneering work, Lord Rayleigh[1] established that materials exhibiting a spatial periodicity may present unusual wave dispersion properties such as frequency bandgaps, where the propagation of waves is forbidden. This periodicity may result from the geometry of the structure,[2] its composition such as in usual phononic crystals[3] but can also be associated with some applied boundary condition.[4,5] More recently, it was also shown that a structure whose physical characteristics such as the permittivity[6,7] or the dimensions[8] vary periodically in time may also possess bandgaps. However, these bandgaps occur in the wave number domain and are oriented vertically in the band structure (i.e., the frequency vs wavenumber diagram) compared to the horizontal frequency bandgaps in conventional spatially periodic media.[9,10] These vertical bandgaps are associated with instabilities, i.e., waves with complex frequencies whose amplitude grows and/or decays everywhere in space due to their exponential time dependence.[9] Periodically time-dependent media may exhibit intriguing wave phenomena. For example, temporal modulation of the refractive index of a photonic system was shown to introduce an effective gauge potential for photons isomorphic to the Aharonov-Bohm effect for electrons.[11] It may be used to create topologically nontrivial properties for photons.[12] Torrent *et al.*[13] have proven that in a dissipative material with time dependent mechanical characteristics, dissipation can be compensated by the amplification of the fields due to the time-dependent properties. Periodicity of the propagation medium may also depend on both time and spatial coordinates.[14] The effect of such space-time modulation on wave propagation was investigated a few decades ago in the context of parametric amplification by Cassedy *et al.*[15] in a linear transmission line made of a series of LC resonators with distributed time-space periodic shunt capacitances. In the last few years, there has been a renewed interest in space-time modulated structures (or STMS) due to their nonreciprocal behavior associated with time reversal symmetry breaking. Indeed, it was shown that the dispersion relation of a medium loses its symmetry with respect to the frequency axis once it is space-time modulated whatever the way this modulation is performed.[16–20] Consequently, dispersion curves of a STMS seem to be "tilted" with respect to their reference configuration in a non-modulated medium.[21] Due to this tilting, directional bandgaps occur[22] i.e., such a medium may exhibit in the same frequency range a stop band for forward propagation and a pass band for

backward propagation and thus behave as a one-way wave propagation device. For example, bulk elastic waves with unidirectional backscattering-immune topological states have been observed in a time-dependent elastic superlattice. The superlattice results from spatial and temporal modulations of the stiffness of the elastic medium that should be achieved experimentally through the photo-softening of a chalcogenide glass.[23] Trainiti *et al.*[22] investigated theoretically the propagation of elastic waves in beams whose density and Young's modulus are periodic functions of time and position. They observed that there exists a critical value of the modulation speed to maximize the nonreciprocal effect. In all these structures, spatiotemporal modulation of their physical characteristics (density and/or elastic moduli) is required.

In a recent paper,[24] we investigated the propagation of longitudinal elastic waves in a one-dimensional structure made of a periodic set of thin piezoelectric rods separated with electrodes and considered the peculiar case where time-dependent electrical boundary conditions are applied to the electrodes. In practice, electrodes are either grounded or left floating, depending on time. Interest devoted to this kind of structure results from their unique bandgap properties even in the time-independent case. They exhibit bandgaps associated only with the charge density located on the electrodes, much larger than those observed in usual one-dimensional elastic or piezoelectric super-lattices.[5] Calculations of transmission coefficients with the help of the finite difference time domain (FDTD) method revealed that a frequency splitting phenomenon occurs in this STMS, i.e., when submitted to an input wave of frequency F_c, the output signal exhibits peaks at frequencies $\pm F_c + n\frac{c_m}{a}$, where n is a signed integer, c_m the modulation speed, and a the distance between two grounded electrodes. This generalized nonlinear phenomenon occurs in any structure that is modulated in time[6,25–27] and is analogous to the classical acousto-optical Brillouin scattering.[28] Additionally, our piezoelectric STMS becomes strongly nonreciprocal, and for specific modulation characteristics, one-way wave propagation can be achieved. Compared to other STMS (see Refs. 10, 22, 23, and 29), the piezoelectric system we proposed does not require a modulation of mechanical characteristics of constituent materials but only changes in time of electrical boundary conditions that can be realized with the help of adequate dynamic electrical circuits.

The present paper also concerns the one-dimensional piezoelectric structure with space-time modulated electrical boundary conditions of Ref. 24. Its purpose is twofold. First, to facilitate STMS design, an analytical model is developed, supplying the dispersion curves of the structure as a function of its geometry, its material properties, and its modulation parameters. The validity of the model is verified by comparison with FDTD simulations results. Second, to investigate the applicative potential of STMS, a series of FDTD simulations is performed to analyze the system behavior in terms of signal transformations.

Consequently, the paper is organized as follows. The characteristics of the piezoelectric STMS are recalled in Sec. II. To gain further insight into the nonlinear phenomena that occur in the STMS and also to analyze rigorously the effect of the modulation speed on the directional bandgaps, we develop in Sec. III a theoretical model to derive an analytical expression of its band structure. This model is built upon the approach proposed by Nassar *et al.*[16] and fully takes into account the piezoelectric properties of the propagating medium. It is validated by comparison with FDTD simulations and its results are discussed in Sec. IV. In Sec. V, several characteristics of strongly nonlinear systems are investigated, such as frequency up and down conversions, wave packet distortions and parasitic echoes. The observations presented in this section shed light on the potential applications of STMS in nonlinear acoustic wave-based components for radio-communication systems. Finally, conclusions are drawn in Sec. VI. An appendix contains the details of the FDTD model adapted to the simulation of the response of an STMS of finite length to an incoming signal. In contrast with the analytical model of Sec. III, all FDTD simulations take into account that, in practice, the number of available electrodes in the piezoelectric propagating medium is limited, and thus changes in electrical boundary conditions are only possible for a discrete set of electrode locations.

II. SYSTEM UNDER STUDY

The system studied in this paper is a one-dimensional stack of identical piezoelectric rods polarized along their length and separated by thin metallic electrodes [see Fig. 1(a)]. Electrodes can be connected to the electrical ground or left floating. It is assumed that rod radius is small enough compared to the wavelength to enable monomode propagation in the frequency range of interest (i.e., there is only one longitudinal mode and no radial mode), and that electrodes are thin enough to neglect their mechanical properties. Poisson effects at the piezoelectric-metal interfaces and losses are also neglected. In all of the following, the distance between two grounded electrodes is always fixed to $a = 1\,\text{cm}$. Rods are made of lead zirconate titanate, with density $\rho = 7450\,\text{kg/m}^3$, elastic stiffness modulus at constant electric field $c^E = 4.3486 \times 10^{10}\,\text{N/m}^2$, piezoelectric constant $e = 25\,\text{C/m}^2$, and dielectric permittivity constant at constant strain $\varepsilon^S = 9.4034 \times 10^{-9}\,\text{F/m}$. With these parameters, the speed of longitudinal waves in the piezoelectric rods is then $c_b = \sqrt{(c^E + e^2/\varepsilon^S)/\rho} = 3842\,\text{m/s}$. On the electrical side, a simple model is assumed, with perfect electrical connections to the ground. This means that electrode potential can

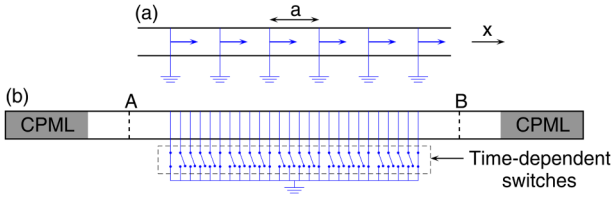

FIG. 1. (a) Schematic view of the piezoelectric crystal considered in the analytical model, i.e., an infinite system with an arbitrarily large number of closely spaced electrodes that can be connected to the ground (connected electrodes in blue), effectively behaving as if the electrical grounds were continuously shifted. (b) Schematic view of the model used in the FDTD calculations. Only a limited number of electrodes are present (in blue), and their connections to the ground are modulated in time and space. For both systems, distance between two grounds is *a*. A and B correspond to either the source location or the transmission measurement point, and "CPML" denotes the Convolution-Perfectly Matched Layers.

instantly change from a given value to zero when an electrode is grounded and that there is no limitation on the electrical currents flowing between an electrode and the ground. In practical implementations of this type of system, the circuits used to create the switchable connections will have to be taken into account. It should be pointed out here that all modulations considered in this paper require only relatively low-frequency electronic circuits. For instance, $c_m = 2000\,\mathrm{m/s}$ with $a = 1\,\mathrm{cm}$ corresponds to a clock frequency of 200 kHz.

An important point of the following models is the concept of equivalent "moving" grounded electrodes. The idea is that the system should include a large set of uniformly spaced individual electrodes, with only a subset connected to the electrical ground at any moment. The subset is then changed as a function of time to simulate a shift of grounded electrodes. It has been demonstrated[5] in the "static" case (i.e., when $c_m = 0$) that floating electrodes have a negligible effect on propagation, and thus only the grounded subset is relevant. The "dynamic" case is more subtle, since an electrode may trap electrical charges when it is disconnected from the ground during operation. However, as electrostatic equilibrium is reached instantaneously, these additional charges on floating electrodes are static and, therefore, can only induce fluctuations of the static polarization field inside the piezoelectric material. In the following, these fluctuations play no role, since only dynamic physical fields are considered.

III. ANALYTICAL MODEL

In the one-dimensional piezoelectric material, the constitutive equations can be written in the form

$$S = s^D T + gD, \tag{1}$$

$$E = -gT + \beta^T D, \tag{2}$$

with S, E, T, and D the dynamic strain, electric field, stress, and electric displacement fields, and s^D, g, and β^T the compliance at constant electric displacement, piezoelectric constant, and impermeability at constant stress. Gauss's law is expressed in any of the piezoelectric elements separated by thin electrodes, giving

$$\frac{\partial D}{\partial x} = 0. \tag{3}$$

Additionally, Newton's law is

$$\frac{\partial T}{\partial x} = \frac{\partial}{\partial t}(\rho v), \tag{4}$$

with ρ and v the material density and particle velocity, respectively. A state vector is defined in the static frame as

$$\boldsymbol{\eta} = \begin{pmatrix} v \\ -T \\ \frac{\partial \varphi}{\partial t} \\ D \end{pmatrix}, \tag{5}$$

with φ the electric potential. Using Eqs. (2)–(4), the space derivative of this state vector may be expressed as

$$\frac{\partial \boldsymbol{\eta}}{\partial x} = \begin{pmatrix} \frac{\partial v}{\partial x} \\ -\frac{\partial T}{\partial x} \\ \frac{\partial^2 \varphi}{\partial x \partial t} \\ \frac{\partial D}{\partial x} \end{pmatrix} = \begin{pmatrix} \frac{\partial S}{\partial t} \\ \frac{\partial}{\partial t}(-\rho v) \\ -\frac{\partial E}{\partial t} \\ 0 \end{pmatrix} = \frac{\partial}{\partial t}\left(-[A]\begin{pmatrix} v \\ -T \\ \frac{\partial \varphi}{\partial t} \\ D \end{pmatrix}\right), \tag{6}$$

with

$$[A] = \begin{pmatrix} 0 & s^D & 0 & -g \\ \rho & 0 & 0 & 0 \\ 0 & g & 0 & \beta^T \\ 0 & 0 & 0 & 0 \end{pmatrix}. \tag{7}$$

Matrix $[A]$ depends on position and time only if space-time modulations of material parameters are considered. Here, it is independent of time, since only space-time modulations of boundary conditions are present. It is assumed in this model that the structure supports a large number of closely spaced electrodes that can be connected to the electrical ground. Therefore, the space-time modulations can be approximated as a continuous shift of regularly-spaced grounded electrodes, with velocity c_m. Let us consider a moving frame of reference traveling with this shift, with spatial and temporal coordinates $(\xi, t) = (x - c_m t, t)$. Time and space derivatives in the moving frame are related to time and space derivatives in the static frame through

$$\left(\frac{\partial}{\partial x}, \frac{\partial}{\partial t}\right) = \left(\frac{\partial}{\partial \xi}, -c_m \frac{\partial}{\partial \xi} + \frac{\partial}{\partial t}\right). \tag{8}$$

As $[A]$ is independent of t, Eq. (6) is rewritten using Eq. (8) as

$$\frac{\partial}{\partial \xi}(([I] - c_m[A])\boldsymbol{\eta}) + [A]\frac{\partial \boldsymbol{\eta}}{\partial t} = 0. \tag{9}$$

Equation (9) takes a standard form if a new state vector $\boldsymbol{\psi} = ([I] - c_m[A])\boldsymbol{\eta}$ is defined, namely,

$$\frac{\partial \boldsymbol{\psi}}{\partial \xi} + [B]\frac{\partial \boldsymbol{\psi}}{\partial t} = 0, \tag{10}$$

with

$$[B] = [A]([I] - c_m[A])^{-1} = \frac{1}{1 - c_m^2 \rho s^D}\begin{pmatrix} c_m \rho s^D & s^D & 0 & -g \\ \rho & c_m \rho s^D & 0 & -c_m \rho g \\ c_m \rho g & g & 0 & \beta^T\left(1 - c_m^2 \rho s^D\right) - c_m^2 g^2 \rho \\ 0 & 0 & 0 & 0 \end{pmatrix}. \tag{11}$$

In the moving frame, the system is a standard spatially periodic medium, and we can look for harmonic solutions subject to the Bloch-Floquet relation, i.e., $\boldsymbol{\psi}(\xi, t) = \boldsymbol{\psi}(\xi)e^{-i\Omega t}$ and $\boldsymbol{\psi}(\xi + a) = \boldsymbol{\psi}(\xi)e^{iKa}$, with Ω and K the angular frequency and wavenumber in the moving frame of reference. The state vector then satisfies $\boldsymbol{\psi}(\xi) = [M_p(\xi, \xi_0)]\boldsymbol{\psi}(\xi_0)$ for any two spatial positions ξ and ξ_0,

with $[M_p]$ being the matricant, which links state vectors at different positions within the piezoelectric elements.

From Eq. (10), it may be deduced that $[M_p(\xi, \xi_0)]$ is the solution of the ordinary differential equation

$$\frac{\partial}{\partial \xi}[M_p(\xi, \xi_0)] = i\Omega[B][M_p(\xi, \xi_0)]. \tag{12}$$

Equation (12) is then simplified into

$$\frac{\partial}{\partial \xi}[N_p(\xi, \xi_0)] = [J][N_p(\xi, \xi_0)], \tag{13}$$

with

$$[N_p(\xi, \xi_0)] = e^{\lambda(\xi-\xi_0)}[M_p(\xi, \xi_0)], \quad \lambda = -i\Omega\frac{c_m}{c_b^2 - c_m^2}, \quad c_b = \frac{1}{\sqrt{\rho s^D}} \quad \text{and} \quad [J] = i\Omega[B] + \lambda[I] \tag{14}$$

Solution of Eq. (13) is then simply $[N_p(\xi, \xi_0)] = e^{[J(\xi-\xi_0)]}$. This matrix exponential can be calculated by different methods. One obtains

$$[N_p(\xi, \xi_0)] = \begin{pmatrix} \cos(\zeta) & ic_b s^D \sin(\zeta) & 0 & -igc_b \sin(\zeta) \\ \frac{i}{c_b s^D}\sin(\zeta) & \cos(\zeta) & 0 & -\frac{g}{s^D}\left(\cos(\zeta) - e^{\lambda(\xi-\xi_0)}\right) \\ \frac{g}{s^D}\left(\cos(\zeta) - e^{\lambda(\xi-\xi_0)}\right) & igc_b \sin(\zeta) & e^{\lambda(\xi-\xi_0)} & i\Omega(\xi-\xi_0)\left(\beta^T + \frac{g^2}{s^D}\right)e^{\lambda(\xi-\xi_0)} - \frac{ig^2 c_b}{s^D}\sin(\zeta) \\ 0 & 0 & 0 & e^{\lambda(\xi-\xi_0)} \end{pmatrix}, \tag{15}$$

with $\zeta = \Omega(\xi - \xi_0)\frac{c_b}{c_b^2 - c_m^2}$. These last expressions allow to calculate $[M_p(\xi = a, \xi_0 = 0)]$.

Matricants can be chained if the cell includes more than one material, or if special boundary conditions are present between cells. Here, two matricants need to be chained, namely, $[M_p(a, 0)]$ representing propagation through a single piezoelectric material of length a and $[M_E]$ corresponding to the passage through an electrode. The product of these two matricants $[M_{cell}] = [M_p][M_E]$ must comply with the Bloch-Floquet relation

$$[M_{cell}] = e^{iKa}[I]. \tag{16}$$

Matricant $[M_E]$ is found using the assumption that electrical electrodes are metallic layers of negligible thickness. Consequently, particle velocity, stress field, and electric potential are continuous across the electrode. Electric displacement D discontinuity across grounded metallic electrodes is related to the electric charge density on the electrode, which does not directly appear in our equation system as a variable. Let us define a variable F_D representing the ratio between D values on both sides of the electrode. M_E then takes the following form:

$$M_E = \begin{pmatrix} 1 & 0 & 0 & 0 \\ 0 & 1 & 0 & 0 \\ 0 & 0 & 1 & 0 \\ 0 & 0 & 0 & F_D \end{pmatrix}. \tag{17}$$

$[M_{cell}] = [M_p][M_E]$ is now expressed entirely as a function of material parameters, F_D, K, and Ω. The fourth line of matrix equation (16) combined with Eqs. (14), (15), and (17) directly gives the value of F_D,

$$F_D = e^{iKa}. \tag{18}$$

The equation system formed by the remaining three lines can be simplified noting that state vectors are always considered at grounded electrode locations. Thus, we can fix $\frac{\partial \varphi}{\partial t} = 0$ and drop this variable. Finally, the existence of a nontrivial solution to this simplified set of equations is equivalent to the vanishing of the determinant of matrix,

$$[M_{sys}] = \begin{pmatrix} M_{cell}^{1,1} - e^{iKa} & M_{cell}^{1,2} & M_{cell}^{1,4} \\ M_{cell}^{2,1} & M_{cell}^{2,2} - e^{iKa} & M_{cell}^{2,4} \\ M_{cell}^{3,1} & M_{cell}^{3,2} & M_{cell}^{3,4} \end{pmatrix}. \tag{19}$$

$\det([M_{sys}]) = 0$ is the dispersion equation. It can be written as

$$\cos\left(Ka - \frac{\Omega a c/c_b}{1-c^2}\right) - \cos(Ka)\frac{k_{33}^2}{1-c^2}\operatorname{sinc}\left(\frac{\Omega a/c_b}{1-c^2}\right) = \cos\left(\frac{\Omega a/c_b}{1-c^2}\right) - \frac{k_{33}^2}{1-c^2}\operatorname{sinc}\left(\frac{\Omega a/c_b}{1-c^2}\right), \tag{20}$$

with $k_{33}^2 = \frac{g^2}{g^2 + \beta^T s^D}$ being the piezoelectric coupling coefficient squared and $c = c_m/c_b$ being the normalized modulation speed. This form reduces to the dispersion relation given in Ref. 5 when $c_m = 0$. Equivalently, the following form can be used:

$$(X-1)^2(Y_+ - Y_-) + 2i\frac{\Omega a}{c_b k_{33}^2}(X - Y_+)(X - Y_-) = 0, \quad \text{with} \quad X = e^{iKa}, \quad Y_+ = e^{-\frac{i\Omega a}{c_b + c_m}}, \quad \text{and} \quad Y_- = e^{\frac{i\Omega a}{c_b - c_m}}. \tag{21}$$

This second form is expressed as a second degree polynomial in X and thus allows finding easily the values of X (and then K) if Ω is known. It should be noted that this dispersion relation is considered in the complex K and complex Ω space. If a given (K, Ω) couple is a solution of the dispersion equation, the corresponding

(k, ω) couple (i.e., wavenumber and frequency in the static frame) is obtained through $k = K$, $\omega = \Omega + c_m k$. As pointed out before, the STMS is a standard space-periodic medium in the moving frame. Therefore, in the moving frame, dispersion branches outside the first Brillouin zone are simple translations of branches in the first Brillouin zone, with translation vectors $(nG, 0)$ (with n a signed integer and G the reciprocal lattice period $2\pi/a$) in the wavenumber-frequency space. However, since the change of variables from (K, Ω) to (k, ω) introduces a progressive frequency shift, dispersion branches in the static frame are invariant by translations of vector (nG, nc_mG). A direct consequence of this property is that dispersion curves for an STMS generally appear as tilted with respect to the unmodulated system.

Among the solutions of the dispersion relation, (k, ω) couples corresponding to exponentially space-growing (negative imaginary part of k) and time-growing (positive imaginary part of ω) amplitudes cannot be discarded *a priori*, since the STMS is an active system with constantly changing connections to the ground behaving as an electrical pump.

IV. ANALYTICAL MODEL RESULTS AND VALIDATION

Figure 2 shows dispersion diagrams (solid black and red lines) obtained for four values of grounded electrode shift velocity c_m, namely, 0 (i.e., the linear case), 500, 1000, and 2000 m/s. Diagrams for negative values of c_m can be obtained by simply flipping the wavenumber axis. These dispersion diagrams are presented in the static frame and thus correspond to (k, ω) couples. As pointed out before, dispersion relation solutions are generally complex. Here, only the solutions with real values of ω (i.e., neither time-growing nor time-decaying) are plotted. Branches with real and complex values of k are distinguished with black and red colors. All diagrams are plotted for values of the real part of k up to $\pm 3\pi/a$. It can be noted that due to the "tilting" of the band structure, there always exists available real wavenumbers for any given frequency [i.e., any horizontal line on Figs. 2(b)–2(d) crosses an infinity of black curves]. For this reason, the notion of "bandgap" is not trivial here, and transmission dips cannot be expected *a priori* even in the presence of branches with complex wavenumbers. Moreover, the coupling process between an incident harmonic signal and any Bloch wave inside the STMS necessarily involves a series of different frequencies. In the following, a "main" dispersion branch will be defined. It is the branch starting at $(k, \omega) = (0, 0)$ and with the phase velocity closest to c_b. In many classical periodic systems, it may be safely assumed that a large part of the energy carried by Bloch waves is associated with wavenumbers located on this branch. This is equivalent to assuming that the Bloch wave is close to a plane wave propagating in a structure with no periodicity. As a consequence, if this hypothesis is correct, the frequency ranges of the complex parts of this main dispersion branch should correspond to transmission dips.

Several important properties can be pointed out in the dispersion diagrams of Fig. 2. First, for the values of c_m considered here, frequency ranges of bandgaps located on the main dispersion branch with positive and negative group velocity become quite different when c_m increases. For $c_m = 500\,\mathrm{m/s}$, there is still a partial frequency overlap, which disappears for $c_m = 1000$ and 2000 m/s. Additionally, dispersion curves show significant deformation. Interestingly, dispersion curve deformations predicted by this model go beyond the changes obtained when considering a simple wavenumber-dependent frequency shift of the $c_m = 0$ case [i.e., considering that the (K, Ω) solutions of the nonlinear case are equal to the (k, ω) of the linear problem, and simply applying $(k, \omega) = (K, \Omega + c_m k)$]. In particular, (a) for the widest bandgaps,

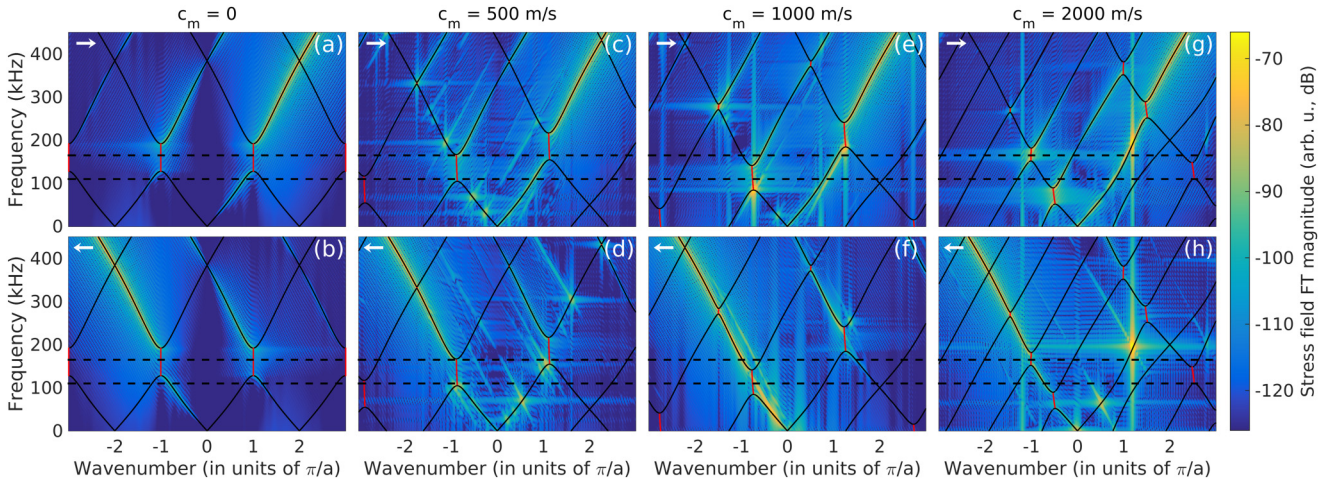

FIG. 2. Space-time Fourier transform of the stress field inside a long STMS for a broadband incident signal and $c_m = 0$ [(a) and (b)], 500 [(c) and (d)], 1000 [(e) and (f)], and 2000 m/s [(g) and (h)], simulated by FDTD. The four top and bottom graphs show results for propagation from A to B and from B to A (as recalled by the white arrows), respectively. All graphs are overlapped with the corresponding dispersion diagrams obtained with the analytical model. The progressive increase of c_m highlights the dispersion branch distortion effect or tilting. Black and red branches correspond to modes with real or complex wavenumbers, respectively. The horizontal axis is the real part of the wavenumber. Horizontal dashed lines show the main frequencies of interest for the following simulated cases, namely, 110 and 165 kHz.

gap boundaries correspond to clearly different wavenumbers, (b) low-frequency group velocities are significantly modified, and (c) for the largest values of c_m, the distance between the two dispersion curves closest to $(k, \omega) = (\pi/a, 2\pi \cdot 100\,\text{kHz})$ is greatly reduced. Property (c) is of special interest, as it can be shown that for even larger values of c_m, those two real branches merge and create a new type of bandgap. However, since in this case the Bloch mode is unstable (time-growing), its study goes beyond the scope of this paper.

To validate this model, it is compared with results obtained with a one-dimensional FDTD code (see Appendix). In FDTD calculations, it is possible to define electrical grounds at every spatial node location, to obtain the same kind of continuous shift as in the analytical model (see Ref. 24). However, since electrode spacing is much coarser in practice, we choose to evaluate STMS performance with five electrodes per period a, i.e., 2 mm-spaced electrodes. At every instant, one electrode out of five is grounded. The grounded set is shifted at fixed time intervals $\Delta t = \frac{a}{5c_m}$.

All simulations consider similar finite 1D systems, namely, an STMS stack with two 10 cm-long piezoelectric bars on its sides, and 5 cm-long CPML (Convolution-Perfectly Matched Layers, see Appendix) regions at both ends. A point stress field source is always placed in one of the piezoelectric bar regions. Figure 1(b) shows a schematic view of the simulated systems. To facilitate the evaluation of the wavenumber content of the modes propagating inside the STMS, a system of length $80a$ is first considered. To highlight full dispersion branches with a single simulation, a broadband source is chosen, namely, a Ricker pulse with central frequency 400 kHz. Figure 2, along with the analytical diagrams, shows the results of a Fourier transform (FT) in time and space for the stress field inside the STMS, over the total simulation time, for four velocities and both propagation directions (source at point A or B, as defined in Fig. 1). The numerical and analytical results agree, both in pass bands and bandgaps. Note that all these FT results support the definition of a main dispersion branch carrying most of the energy, as defined previously.

In addition to the dispersion branches predicted by the analytical model, Fig. 2 also exhibits much weaker ones [oblique lines most visible in Figs. 2(c) and 2(d)], as well as some bright spots [for instance around $(k, \omega) = (1.2\pi/a, 2\pi \cdot 195\,\text{kHz})$ in Fig. 2(g)]. These features are absent from simulations that consider quasicontinuous shifts for the grounded electrode locations. Part of the problem can be explained by noting that if electrode separation is $a/5$, then any spatiotemporal modulation with velocity c_m is strictly equivalent to the modulation with velocity $-4c_m$. In other words, a shift of one fifth of a period in one direction is equivalent to a shift of four fifths in the opposite one. This simple argument shows that secondary dispersion branches can be excited in this type of system. It can also explain the additional bright spots that are usually associated with unstable regimes. Here, for instance, $c_m = 2000\,\text{m/s}$ is stable, but $-4c_m = -8000\,\text{m/s}$ is strongly unstable (supersonic regime[30]).

V. SIGNAL DISTORTION ANALYSIS

Dispersion relations calculated with the analytical model provide information about the available propagation modes inside the structure, but do not give direct insight concerning the coupling process at the STMS interfaces, and consequently its signal transmission properties. First, as pointed out before, by construction, the system exhibits frequency conversion phenomena, since Bloch modes in time-space modulated media contain a series of frequencies. It has been shown[31] that these phenomena can become quite significant in the case of elastic beams presenting a space-time modulation of Young's modulus. Up and down frequency conversions generally occur both inside the system and at its interfaces. Different applications may be targeted depending on conversion efficiency. A STMS with strong conversion efficiency could be used in a frequency synthesizer, whereas minimal frequency conversion would be preferable for the realization of nonreciprocal components. Additionally, signal distortion should be verified directly for wave packets transmitted through the system. Phase characteristics and the existence of parasitic echoes are especially important for potential radio-communication applications.

To study these effects, the FDTD code is exploited. The previously described finite system is simulated again, this time with a length of $14a$, and with different pulse or harmonic incident signals.

Figure 3 shows the simulated stress field amplitude as a function of time t and position x in the system for different values of c_m, and different drives. The CPML regions on the sides of the simulation domain exhibit evanescent fields and are hidden in this figure, for clarity. In all cases, the source is an added stress field located at the point indicated by a vertical solid line, 5 cm away

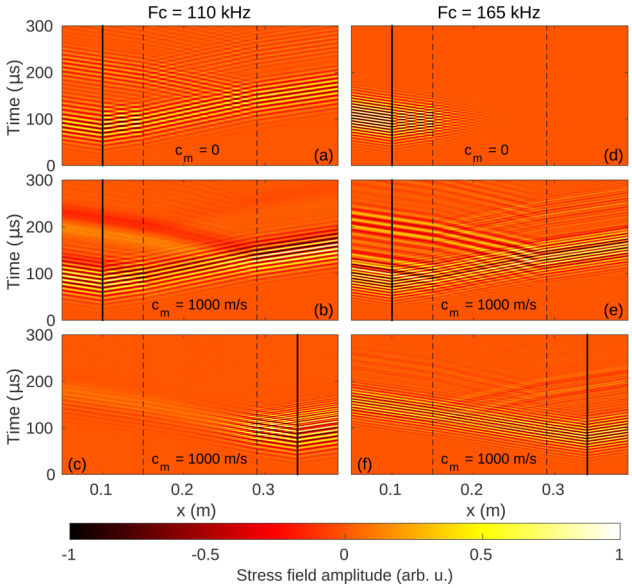

FIG. 3. Stress field amplitude as a function of time and position in the STMS, for pulse signals with center frequencies $F_c = 110$ kHz [(a)–(c)] or 165 kHz [(d)–(f)] emitted from the left [(a), (b), (d), and (e)] or from the right [(c) and (f)], and for $c_m = 0$ [(a) and (d)] or 1000 m/s [(b), (c), (e), and (f)]. The modulated piezoelectric structure is located between the dashed lines. The source location is shown with a solid line.

from the device region. Its time evolution corresponds to a gaussian pulse with center frequency either 110 or 165 kHz. The two top graphs serve as a reference, showing field patterns in the (linear) $c_m = 0$ case for the two different incident pulse signals. Since a bandgap is present only in the 130–190 kHz range in this case, the pulse centered on 165 kHz is strongly reflected at the STMS input interface (dashed vertical line on the left), whereas the pulse centered on 110 kHz is partly transmitted. In the latter case, in the STMS, changes in both group and phase velocities are clearly visible [they correspond to pulse peak and phase front slopes in (x, t) graphs], as well as multiple pulse reflections due to the effective impedance mismatch between the STMS and the surrounding homogeneous piezoelectric medium. The four bottom graphs show results for $c_m = 1000$ m/s, the same two incident pulse signals as before, and for sources located either on the left or on the right. For $c_m = 1000$ m/s and the pulse centered around 110 kHz, a strong nonreciprocity effect can be noted. The pulse incident on the left propagates through the system, with field patterns roughly similar to those obtained for $c_m = 0$. On the other hand, the pulse incident on the right is strongly reflected, with most of the energy inside the structure localized within the first few cells. For $c_m = 1000$ m/s and the pulse centered around 165 kHz, the bandgap effect evidenced in the linear case disappears. For both source locations, the pulse is transmitted through the structure. However, field patterns for the source on the right [Fig. 3(f)] are clearly not a mirror image of those for the source on the left [Fig. 3(e)]. In particular, the frequency of the signal reflected at the output interface is lower in the latter.

The strong reflection at the STMS input side in Fig. 3(c) shows that, at least in this case, the coupling mechanism at an STMS-piezoelectric bar interface is dominated by the main dispersion branch previously defined. In other words, when the frequency of an incident signal is inside of a main branch bandgap, it is reflected and does not couple to Bloch waves with same frequency but larger wavenumbers.

To further analyze the STMS influence on pulse signals, stress field amplitude at a point located 5 cm away from the structure on its output side is plotted in Fig. 4 (in blue) for the six cases of Fig. 3. On all graphs, the signal probed when the STMS is replaced by a homogeneous piezoelectric material of the same length is shown in red. Since group delays are generally different in each case, an additional time shift (Δt) is artificially added on those reference signals to highlight their similarities with or differences from those which have been transmitted through the STMS. Transmitted signals for $c_m = 0$ and incident pulses centered around 110 [Fig. 4(a)] and 165 kHz [Fig. 4(d)] show the expected behavior for transmission through a periodic structure outside and inside of a Bragg bandgap, respectively. In Fig. 4(a), the second echo is quite visible, confirming the impedance mismatch between STMS and surrounding medium and thus the creation of reflected pulses at its interfaces, even in this linear case. Among the four other plotted signals ($c_m \neq 0$), only Fig. 4(c) exhibits a suppressed transmission, in agreement with Fig. 3(c), whereas Figs. 4(b), 4(e), and 4(f) show limited signal distortion with respect to the reference (in red), apart from slightly different group delays and a weaker second echo. Figure 4(b) is particularly interesting since it corresponds to a case where the second echo is actually weaker for $c_m = 1000$ m/s than for $c_m = 0$. The fact that different echoes are affected differently by the STMS is a direct consequence of its nonreciprocal transmission properties and corresponds to a form of backscattering immunity effect: whereas the first echo propagates once "downstream" (with respect to electrode shift), the second propagates twice downstream and once "upstream." This kind of property could be exploited in applications where parasitic echoes are to be minimized even though impedance matching cannot be ensured.

Figure 5 shows amplitude and phase data for the transmitted pulses presented in Fig. 4. Amplitude data show that the transmission coefficient contrast between forward and backward directions for $c_m = 1000$ m/s can reach about 20 dB around

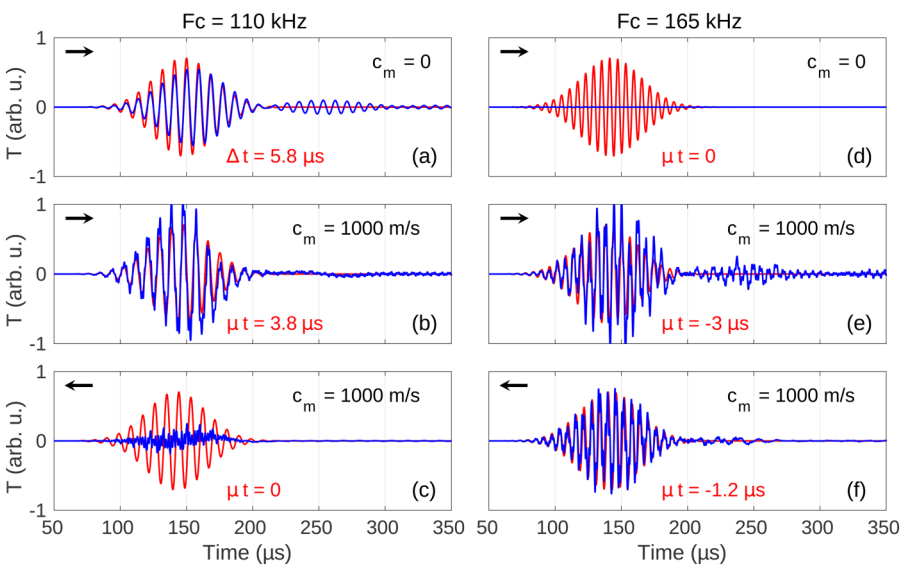

FIG. 4. Stress field amplitude as a function of time, probed at a point located 5 cm away from the STMS on its output side, for pulse signals with center frequencies $F_c = 110$ kHz [(a)–(c)] or 165 kHz [(d)–(f)] emitted from the left [(a), (b), (d), and (e)] or from the right [(c) and (f)], and for $c_m = 0$ [(a) and (d)] or 1000 m/s [(b), (c), (e) and (f)]. The signal in red is a time-shifted reference (see text).

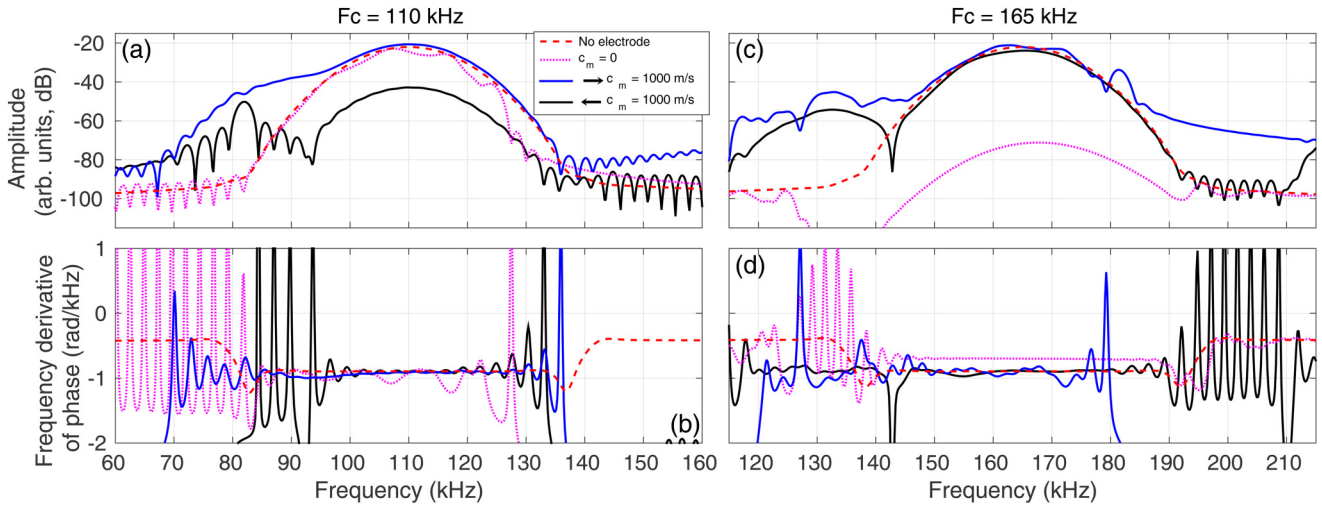

FIG. 5. Stress field magnitude [(a) and (c)] and phase [(b) and (d)] data corresponding to the time data of Fig. 4 for the pulse signals with center frequencies $F_c = 110$ kHz [(a) and (b)] and $F_c = 165$ kHz [(c) and (d)]. In each panel, the four curves correspond to $c_m = 0$ (dotted magenta line), $c_m = 1000$ m/s with a propagation direction from left to right (solid blue line), from right to left (solid black line) and the reference obtained by replacing the STMS by a simple piezoelectric bar of same length (dashed red line).

110 kHz [Fig. 5(a)]. Frequency conversion effects are not negligible in this case (for example, around 80 kHz). For the pulse centered on 165 kHz [Fig. 5(c)], gaussian pulse shape is remarkably similar between both forward and backward cases for $c_m = 1000$ m/s and the system without any grounded electrode. This is consistent with the previous observations on time signals: in some cases, the space-time modulation can actually "reduce" the influence of the periodically-spaced grounded electrodes. As pointed out before, the

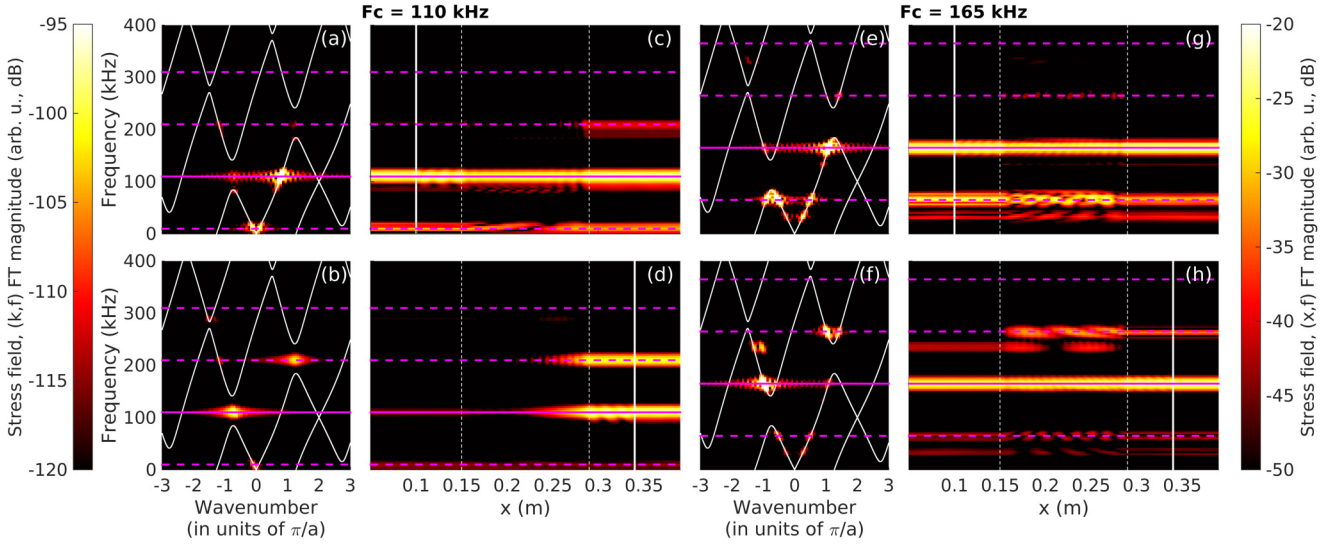

FIG. 6. Magnitude of space-frequency domain [(c), (d), (g), and (h)] and wavenumber-frequency domain [(a), (b), (e), and (f)] Fourier transforms of stress field data are shown in Fig. 3, for the pulse signals with center frequency $F_c = 110$ kHz [(a)–(d)] or 165 kHz [(e)–(h)] emitted from the left [(a), (c), (e), and (g)] or from the right [(b), (d), (f), and (h)], only for $c_m = 1000$ m/s. Vertical dashed and solid lines in the space-frequency domain graphs are the same as in Fig. 3. Analytical dispersion curves (real part only) are reproduced in white in the wavenumber-frequency domain graphs. The horizontal solid and dashed lines show the incident center frequency F_c and the Brillouin scattered frequencies $F_c + n\frac{c_m}{a}$ (n being an integer), respectively. Note that for the wavenumber-frequency Fourier transform, only the STMS region is considered.

periodic structures under study are always dispersive, and they introduce time delays with respect to propagation in a simple medium. However, provided that their transmission properties in phase are simple enough, they could still prove useful for the realization of (nonlinear) components. Figures 5(b) and 5(d) show the frequency derivative of the phase of the same time signals as before. For the two gaussian pulses considered, phase evolution is remarkably linear around the center frequency.

Frequency conversion effects in the STMS can also be studied by repeating the time-domain Fourier transform of Fig. 5 for each FDTD node location, as shown in Figs. 6(c), 6(d), 6(g), and 6(h) for c_m = 1000 m/s only, or by applying a double space-time Fourier transform similar to that of Fig. 2, as shown in Figs. 6(a), 6(b), 6(e), and 6(f). These figures show energy repartition in frequency and real space or reciprocal (wavenumber) space, over the entire duration of the simulation. They help identifying and localizing all frequency conversion effects occurring in the system. As pointed out before, frequency conversions can only occur between a given frequency f and frequencies $\pm f + nc_m/a$ with n being a (signed) integer. For the pulse signal with center frequency $F_c = 110$ kHz, forward and backward transmissions are accompanied by significant down (from 110 kHz to 10 kHz) and up (from 110 kHz to 210 kHz) conversion effects, respectively. An important point is that for backward transmission, the up-converted signal is not transmitted. It is only present in the reflection on the input interface and, consequently, does not affect the unidirectional transmission of energy. For the pulse signal with frequency $F_c = 165$ kHz, the same general properties are observed, even though it corresponds to a pass band for both directions in this case. Note that in Figs. 6(g) and 6(h), small signals are generated around 35 and 235 kHz, respectively. They correspond to frequency conversions from $F_c = 165$ kHz to $-F_c + 2c_m/a = 35$ kHz and $-F_c + 4c_m/a = 235$ kHz, respectively. It should be noted that these results do not give much information about the exact locations where frequency conversions occur in the system, at least in the general case. Figure 6(d) clearly shows that a strong frequency conversion effect occurs at the input interface, but is a special case, since the Bloch wave is evanescent inside the STMS. Calculations with sliding window time Fourier transforms (not presented here) show that in general, frequency conversions occur at input and output interfaces, and also inside the STMS.

Up to this point, we focused on a few specific operation regimes (i.e., choices of c_m and F_c), but the models presented here can be exploited in parametric studies. For instance, the analytical model of Sec. III can be used to calculate the wavenumber imaginary part for the main dispersion branch as a function of frequency and modulation speed [Fig. 7(a)]. To simplify this parametric study, the dispersion relation is used in its second form [Eq. (21)], setting a real Ω and solving for K. This means that inside bandgaps, there exists an imaginary part of frequency (in the static frame) for plotted solutions (since $\omega = \Omega + c_m k$ and k is complex). However, it can be shown that for the system under study, these solutions are very close to those with real frequencies ω and complex wavenumbers k. This analytical parametric study can be compared with FDTD parametric studies, using exactly the same setup as in Figs. 3–6, but with harmonic incident signals. In these calculations, the parameter of interest is the fundamental frequency

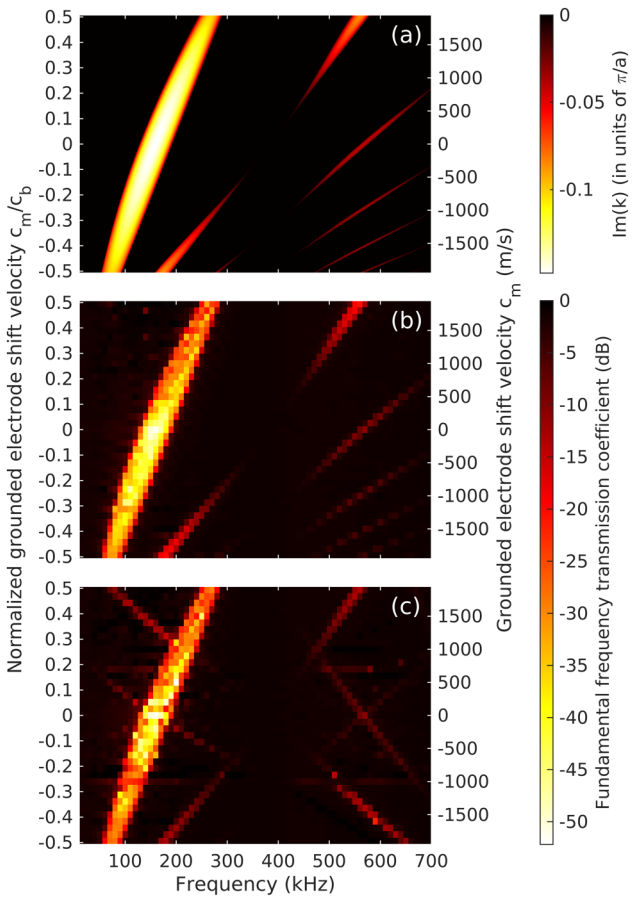

FIG. 7. (a) Imaginary part of wavenumber k for the main dispersion branch, obtained with the analytical model, as a function of frequency in the static frame and c_m in normalized (left axis, c_m/c_b) and absolute (right axis) units. FFTC as a function of fundamental frequency and c_m (or c_m/c_b) (b) for continuous grounded electrode shifts (reproduced from Ref. 24) and (c) for the same discrete set of 2 mm-spaced electrodes as in Figs. 3–6.

transmission coefficient (FFTC) magnitude for harmonic incident signals of different frequencies and for different values of c_m. The parametric study result for continuous grounded electrode shifts was already presented in Ref. 24 and is reproduced here in Fig. 7(b) for comparison purposes. The similarity between the two graphs traduces the strong influence of the main dispersion branch bandgaps on the STMS transmission properties. Finally, Fig. 7(c) shows the FFTC spectra for the model considered in the current paper, i.e., with 2 mm-spaced electrodes. Again, the main FFTC features are strongly correlated with the predictions of the analytical model. Secondary transmission dips also appear, and their frequencies generally decrease when c_m increases, in opposition with the main dips. Even though the analytical model of Sec. III is insufficient to predict these secondary dips, the general explanation is the same as for the secondary branches of Fig. 3, namely, that discrete shifts cannot be associated with a single modulation velocity.

TABLE I. Values of fundamental frequency transmission coefficients (FFTC) and frequency conversion transmission coefficients (FCTC) considering harmonic signals of frequency $F_c = 110$ kHz or 165 kHz, for $c_m = 0$ and for $c_m = 1000$ m/s with both propagation directions. FCTC values are given for the first higher and lower harmonics, i.e., $F_c + n\frac{c_m}{a}$ with $n = +1$ and -1, respectively. "N.A." indicates that the FCTC calculation is not applicable to the unmodulated case.

	FFTC (dB)		FCTC $n = +1$ (dB)		FCTC $n = -1$ (dB)	
c_m and direction	$F_c = 110$ kHz	$F_c = 165$ kHz	$F_c = 110$ kHz	$F_c = 165$ kHz	$F_c = 110$ kHz	$F_c = 165$ kHz
$c_m = 0$	−3.76	−50.18	N.A.	N.A.	N.A.	N.A.
$c_m = 1000$ m/s, A to B	−0.74	−1.92	−17.68	−31.74	−9.91	−9.87
$c_m = 1000$ m/s, B to A	−22.85	−3.91	−22.94	−21.99	−28.29	−31.00

Finally, based on these FDTD calculations with harmonic signals, it is possible to quantify transmission efficiency for the previously studied cases. Transmission efficiency for the fundamental frequency is the FFTC. Table I summarizes the values obtained for the unmodulated case and for $c_m = 1000\,\mathrm{m/s}$, considering propagation from A to B or from B to A, for $F_c = 110\,\mathrm{kHz}$ and 165 kHz. Additionally, transmission efficiency for frequency converted signals can be defined as the magnitude of the transmitted field at frequency $F_c + n\frac{c_m}{a}$ normalized by the source amplitude at F_c. This quantity, labeled frequency conversion transmission coefficient (FCTC), is also shown in Table I, for the same cases as before, and for $n = +1$ and -1. Both FFTC and FCTC values obtained with harmonic signals are consistent with the observations based on Figs. 3–6, which used gaussian pulse signals.

VI. SUMMARY AND CONCLUSION

We investigated the propagation of longitudinal acoustic waves in a one-dimensional structure made of a periodic set of finite piezoelectric rods separated with electrodes and considered the peculiar case where time-dependent electrical boundary conditions are applied to the electrodes. An analytical model is proposed that allows writing closed form solutions of the dispersion relation of such STMS. The model evidenced the tilting of the band structure with respect to their reference configuration in a nonmodulated medium that strongly depends on the modulus and the direction of the modulation speed vector. Due to the tilting, such a medium may exhibit in the same range of frequency, a stop band for forward propagation and a pass band in the opposite direction. This nonreciprocal behavior results from time symmetry breaking associated with the temporal modulation of the electrical boundary conditions. The structure with a nonreciprocal behavior behaves as a one-way wave propagation device and may have many potential technological applications. Beyond the case of the piezoelectric STMS studied here, it should be noted that the general principle of the developed model could be applied in different wave physics problems with space-time modulations of boundary conditions. For instance, it could be adapted for the study of piezomagnetic phononic crystals,[32] or more generally acoustic wave propagation in systems with modulated mechanical boundary conditions, such as moving support points. In addition to the analytical model development, with the aim of studying the effect of the space-time modulation on an acoustic wave propagating through the finite structure, we performed FDTD numerical calculations that predict accurately the system response to incoming signals. Nonlinear phenomena that may have important consequences for the potential applications of STMS, such as frequency up and down conversions, wave packet distortions, and parasitic echoes, were also analyzed. In particular, limited distortion of "passing" signal was evidenced in the one-way propagation configuration.

Compared to other space-time modulated structures,[22,23,29] the proposed piezoelectric system does not require a modulation of mechanical characteristics of constituent materials but only changes in time of electrical boundary conditions that can be realized with the help of adequate dynamic electrical circuits. This should facilitate the manufacturing of one-way wave propagation devices.

APPENDIX: FINITE DIFFERENCE TIME DOMAIN MODEL

In the piezoelectric medium, physical equations used for the FDTD model are Gauss's law [Eq. (3)], Newton's law [Eq. (4)], and equations of piezoelectricity with independent variables $S = \frac{\partial u}{\partial x}$ and $E = -\frac{\partial \varphi}{\partial x}$

$$T = c^E \frac{\partial u}{\partial x} + e\frac{\partial \varphi}{\partial x}, \tag{A1}$$

$$D = e\frac{\partial u}{\partial x} - \epsilon^S \frac{\partial \varphi}{\partial x}, \tag{A2}$$

where u is the particle displacement, e the piezoelectric constant, and ϵ^S the dielectric permittivity at constant strain. v, T, $\dot{D}$, and $\dot{\phi}$ are chosen as state variables where $\dot{}$ denotes partial derivative as a function of time. Equations (3), (A1), and (A2) are, respectively, written as

$$\frac{\partial \dot{D}}{\partial x} = 0, \tag{A3}$$

$$\frac{\partial T}{\partial t} = c^E \frac{\partial v}{\partial x} + e\frac{\partial \dot{\varphi}}{\partial x}, \tag{A4}$$

$$\dot{D} = e\frac{\partial v}{\partial x} - \epsilon^S \frac{\partial \dot{\varphi}}{\partial x}. \tag{A5}$$

Infinitely thin electrodes located between the piezoelectric elements are represented by equations relating the mechanical and electric fields at both sides of the electrodes

$$T^+ = T^-, \quad v^+ = v^-, \quad \dot{D}^+ = \dot{D}^- \tag{A6}$$

for a floating electrode and

$$T^+ = T^-, \quad v^+ = v^-, \quad \dot{D}^+ - \dot{D}^- = \dot{\sigma}, \tag{A7}$$

where σ is the free charge surface density on the grounded electrode. These equations are discretized with the Yee algorithm.[33] Specific Convolution-Perfectly Matched Layers[34,35] are used at both ends of the discretization mesh to alleviate unwanted reflection of waves on these ends. At time step $t^n = n\Delta t$, we compute firstly velocity at each space grid point i using discretized Newton's equation

$$V_i^n = V_i^{n-1} + m_i \frac{\Delta t}{\Delta x}\left(T_{i+1}^{n-\frac{1}{2}} - T_i^{n-\frac{1}{2}}\right) + m_{Ai} A_i^{n-1}, \tag{A8}$$

where Δx is the grid spacing and m_i the mass term associated to grid point i. m_{Ai} and A_i are, respectively, the memory coefficient and the memory variable at grid point i inside the CPML zone and vanish elsewhere. Secondly, time derivative of electric potential is obtained for all space grid points using the equation of electrostatics

$$\dot{\boldsymbol{\Phi}}^{\boldsymbol{n}} = [M_\epsilon]^{-1}\left([M_\epsilon]\boldsymbol{V}^{\boldsymbol{n}} + [M_B]\boldsymbol{B}^{\boldsymbol{n}} + [M_C]\boldsymbol{C}^{\boldsymbol{n}} - \dot{\boldsymbol{\Sigma}}^{\boldsymbol{n}}\right), \tag{A9}$$

which is obtained by discretizing and combining Eqs. (A3) and (A5). $\dot{\boldsymbol{\Phi}}^{\boldsymbol{n}}$, $\boldsymbol{V}^{\boldsymbol{n}}$, and $\dot{\boldsymbol{\Sigma}}^{\boldsymbol{n}}$ are the vectors containing the values of $\dot{\phi}$, v, and $\dot{\sigma}$ for all space grid points at time step t^n. Vectors $\boldsymbol{B}^{\boldsymbol{n}}$ and $\boldsymbol{C}^{\boldsymbol{n}}$ contain the values of memory variables at time step t^n for space grid points inside the CPML zone and zeros otherwise. It may be noted that the change of boundary condition on the electrodes vs time is introduced via Eq. (A9) by prescribing $\dot{\Phi}_i^n = 0$ (grounded case) or $\dot{\Sigma}_i^n = 0$ (floating case) at each grid point corresponding to an electrode. Finally, the stress at each space grid point i is evaluated at time step $t^{n+\frac{1}{2}}$ using the discretized equation issued from Eq. (A4),

$$T_i^{n+\frac{1}{2}} = T_i^{n-\frac{1}{2}} + k_i \frac{\Delta t}{\Delta x}\left(V_i^n - V_{i-1}^n\right) + p_i \frac{\Delta t}{\Delta x}\left(\dot{\Phi}_i^n - \dot{\Phi}_{i-1}^n\right) + m_{Bi} B_i^{n-\frac{1}{2}} + m_{Ci} C_i^{n-\frac{1}{2}}, \tag{A10}$$

where k_i and p_i are, respectively, stiffness and piezoelectric terms associated to grid points i.

REFERENCES

[1] L. Rayleigh, Philos. Mag. **24**, 145 (1887).
[2] A. Díaz-de Anda, A. Pimentel, J. Flores, A. Morales, L. Gutiérrez, and R. A. Méndez-Sánchez, J. Acoust. Soc. Am. **117**, 2814 (2005).
[3] P. Deymier, *Acoustic Metamaterials and Phononic Crystals*, Springer Series in Solid-State Sciences Vol. 173 (Springer, Berlin, 2013).
[4] D. Mead, J. Sound Vibr. **104**, 9 (1986).
[5] S. Degraeve, C. Granger, B. Dubus, J. O. Vasseur, M. Pham Thi, and A.-C. Hladky-Hennion, J. Appl. Phys. **115**, 194508 (2014).
[6] J. R. Zurita-Sánchez, P. Halevi, and J. C. Cervantes-González, Phys. Rev. A **79**, 053821 (2009).
[7] N. Wang, Z.-Q. Zhang, and C. T. Chan, Phys. Rev. B **98**, 085142 (2018).
[8] D. W. Wright and R. S. C. Cobbold, Smart Mater. Struct. **18**, 015008 (2009).
[9] S. Taravati, N. Chamanara, and C. Caloz, Phys. Rev. B **96**, 165144 (2017).
[10] G. Trainiti, Y. Xia, J. Marconi, G. Cazzulani, A. Erturk, and M. Ruzzene, Phys. Rev. Lett. **122**, 124301 (2019).
[11] K. Fang, Z. Yu, and S. Fan, Phys. Rev. Lett. **108**, 153901 (2012).
[12] L. Yuan, S. Xu, and S. Fan, Opt. Lett. **40**, 5140 (2015).
[13] D. Torrent, W. J. Parnell, and A. N. Norris, Phys. Rev. B **97**, 014105 (2018).
[14] N. Chamanara, Z.-L. Deck-Léger, C. Caloz, and D. Kalluri, Phys. Rev. A **97**, 063829 (2018).
[15] E. S. Cassedy and A. A. Oliner, Proc. IEEE **51**, 1342 (1963).
[16] H. Nassar, H. Chen, A. N. Norris, M. R. Haberman, and G. L. Huang, Proc. R. Soc. A **473**, 20170188 (2017).
[17] J. Vila, R. K. Pal, M. Ruzzene, and G. Trainiti, J. Sound Vibr. **406**, 363 (2017).
[18] H. Nassar, X. Xu, A. Norris, and G. Huang, J. Mech. Phys. Solids **101**, 10 (2017).
[19] E. Riva, J. Marconi, G. Cazzulani, and F. Braghin, J. Sound Vibr. **449**, 172 (2019).
[20] J. Huang and X. Zhou, Int. J. Solids Struct. **164**, 25 (2019).
[21] H. Nassar, H. Chen, A. N. Norris, and G. L. Huang, Phys. Rev. B **97**, 014305 (2018).
[22] G. Trainiti and M. Ruzzene, New J. Phys. **18**, 083047 (2016).
[23] N. Swinteck, S. Matsuo, K. Runge, J. O. Vasseur, P. Lucas, and P. A. Deymier, J. Appl. Phys. **118**, 063103 (2015).
[24] C. Croënne, J. O. Vasseur, O. Bou Matar, M.-F. Ponge, P. A. Deymier, A.-C. Hladky-Hennion, and B. Dubus, Appl. Phys. Lett. **110**, 061901 (2017).
[25] K. Yi, S. Karkar, and M. Collet, J. Sound Vibr. **429**, 162 (2018).
[26] S. Mezil, N. Chigarev, V. Tournat, and V. Gusev, Ultrasonics **69**, 225 (2016).
[27] F. Li, C. Chong, J. Yang, P. G. Kevrekidis, and C. Daraio, Phys. Rev. E **90**, 053201 (2014).
[28] S. Y. Elnaggar and G. N. Milford, IEEE Trans. Antennas Propag. **66**, 3500 (2018).
[29] M. H. Ansari, M. A. Attarzadeh, M. Nouh, and M. A. Karami, Smart Mater. Struct. **27**, 015030 (2018).
[30] E. S. Cassedy, Proc. IEEE **55**, 1154 (1967).
[31] K. Yi, M. Collet, and S. Karkar, Phys. Rev. B **96**, 104110 (2017).
[32] M.-F. Ponge, C. Croënne, J. O. Vasseur, O. Bou Matar, A.-C. Hladky-Hennion, and B. Dubus, J. Acoust. Soc. Am. **139**, 3288 (2016).
[33] A. Taflove, *Computational Electrodynamics—The Finite Difference Time Domain Method* (Artech House Inc., Norwood, 1995).
[34] O. Bou Matar, V. Preobrazhensky, and P. Pernod, J. Acoust. Soc. Am. **118**, 2880 (2005).
[35] Y. Li, O. Bou Matar, V. Preobrazhensky, and P. Pernod, in *2008 IEEE International Ultrasonics Symposium Proceedings* (IEEE, 2008), p. 1568.